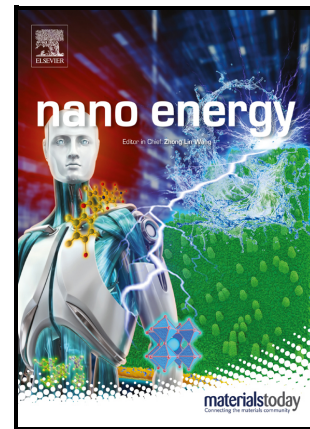


Triboelectric Nanogenerator-embedded Intelligent Bearing with Rolling Ball Defect Diagnosis via Signal Decomposition and Automated Machine Learning

Fangyang Dong, Hengyi Yang, Hengxu Du, Meixian Zhu, Ziyue Xi, Yulian Wang, Taili Du, Minyi Xu



PII: S2211-2855(23)00909-6

DOI: <https://doi.org/10.1016/j.nanoen.2023.109072>

Reference: NANOEN109072

To appear in: *Nano Energy*

Received date: 28 August 2023

Revised date: 1 November 2023

Accepted date: 5 November 2023

Please cite this article as: Fangyang Dong, Hengyi Yang, Hengxu Du, Meixian Zhu, Ziyue Xi, Yulian Wang, Taili Du and Minyi Xu, Triboelectric Nanogenerator-embedded Intelligent Bearing with Rolling Ball Defect Diagnosis via Signal Decomposition and Automated Machine Learning, *Nano Energy*, (2023) doi:<https://doi.org/10.1016/j.nanoen.2023.109072>

This is a PDF file of an article that has undergone enhancements after acceptance, such as the addition of a cover page and metadata, and formatting for readability, but it is not yet the definitive version of record. This version will undergo additional copyediting, typesetting and review before it is published in its final form, but we are providing this version to give early visibility of the article. Please note that, during the production process, errors may be discovered which could affect the content, and all legal disclaimers that apply to the journal pertain.

Triboelectric Nanogenerator-embedded Intelligent Bearing with Rolling Ball Defect Diagnosis via Signal Decomposition and Automated Machine Learning

Fangyang Dong, Hengyi Yang, Hengxu Du, Meixian Zhu, Ziyue Xi, Yulian Wang, Taili Du, and
Minyi Xu**

Fangyang Dong and Hengyi Yang contributed equally to this work.

F. Dong, H. Yang, H. Du, Z. Xi, Y. Wang, T. Du, M. Xu
Dalian Key Lab of Marine Micro/Nano Energy and Self-Powered Systems, Marine Engineering
College, Dalian Maritime University, Dalian 116026, China
E-mail: dutaili@dmlu.edu.cn; xuminyi@dmlu.edu.cn

M. Zhu, T. Du

Collaborative Innovation Research Institute of Autonomous Ship, Dalian Maritime University,
Dalian 116026, China

Keywords: bearing ball defect, fault diagnosis, triboelectric nanogenerators, signal decomposition,
automated machine learning

Abstract: Smart fault diagnosis of bearings is of great significance due to their extensive applications on various occasions. Recently, self-powered sensing technology based on triboelectric nanogenerators promotes the development of intelligent bearings. However, the effective detection and recognition of the rolling element defects of bearings need to be investigated further. This study proposes a triboelectric sensor-embedded rolling bearing (T-bearing) to monitor the working conditions and conduct the defect diagnosis of rolling balls. The

interdigitated copper electrode covered by polytetrafluoroethylene film is attached to the inner surface of the outer ring of a commercial bearing. Such a design not only directly forms the TENG with rolling balls to obtain the contact-sensing signals, but also successfully achieves the diagnosis of rolling ball defects with similar triboelectric signals through a novel analysis and prediction paradigm combining signal decomposition and automated machine learning. Finally, a recognition accuracy of 99.48% with five different conditions of bearing balls is reached, which is extremely superior to the highest accuracy of 78.34% without signal decomposition. Thus, this study provides a new strategy for the defect diagnosis and the intelligent application of triboelectric bearings.

1. Introduction

Bearings, which serve as a vital component in industrial and daily life applications, plays a crucial role in the long-term reliable operation of the rotating machinery [1, 2]. Economic losses or even human casualties would be bought out in addition to significant disruptions of the performance and lifetime of the machinery once failures of bearing emerge. The failures of the bearing may be caused by fatigue, insufficient lubrication, contamination, etc. [3]. Researchers embedded sensing nodes into the housing for self-sensing to achieve intelligent bearing as early as 1990s [4, 5]. Real-time working condition monitoring of the bearing and abnormal condition detection is achieved by the sensor arrangement and data processing method to some extent. Since then, a few intelligent bearing prototypes have been presented with the development and broad application of the Internet of Things (IoT) and big-data processing technologies. However, these bearings require the additional sensors and systems, which increases structural complexity and relies on external power supply, limiting their large-scale application.

Triboelectric nanogenerator (TENG), based on the contact electrification and electrostatic induction, can effectively convert mechanical energy into electrical energy, has gained obvious technology evolution since it was proposed one decade ago [6]. Because of the high sensitivity to the mechanical excitation, triboelectric sensors have become the most popular and promising research trend for practical applications. The output of TENG can respond quickly to variations in the testing condition, such as vibration frequency [7], flow velocity [8], and rotating angle [9]. Furthermore, triboelectric sensors that can generate sensing electrical signals independently have unique advantages in a limited energy supply [10]. Therefore, the rolling-type free-standing layer TENG with comparable movement mode has been developed as a self-powered bearing to sense the rotation [11-13]. Driven by the practicality, some triboelectric sensors designed for real bearings are proposed [14-17]. Han et al. [14] pasted interdigital electrodes on the bearing's outer ring to maintain the structural integrity of the bearing. Gao et al. [15] and Jiang et al. [16] set interdigital electrodes on the bearing end cover to ensure compact structure of the proposed bearings. Gao et al. [17] coated the steel shaft with Si-incorporated diamond-like carbon films for a commercial metal-polymer plain bearing to keep the super durability and load capability. These designs play an important role in promoting the application of triboelectric technology on the bearings.

At present, the function of most sensors is realized by analyzing the time-domain data of the collected sensing signals, usually by the magnitude and frequency [18, 19]. But this preliminary analytics approach may lose important features hidden in the sensing signals, such as the weak fluctuations caused by the faults. To extract the full sensory information, advanced artificial intelligence (AI) technology using machine learning (ML)-assisted data analytics can be applied [20, 21]. Zhao et al. [22] designed a highly sensitive triboelectric vibration sensor to monitor the

operating conditions of a mechanical gear system, reaching a recognition rate of 99.78 % with the frequency-domain signals from several fault conditions of the gearbox. Han et al. [23] obtained the fault characteristic frequency of the TENG output current when the triboelectric rolling bearing has the component faults. By utilizing ML algorithms, the classification accuracies can exceed 92%. Jiang et al. [16] proposed a ribbon-cage-based triboelectric bearing to perform the fault diagnosis of gears and bearings, and the classification accuracy can exceed 90% combined with the time-frequency transformation and deep learning (DL) algorithm. Especially, Gao et al. and Choi et al. were concerned about the monitoring of rolling elements in their works [13, 17]. Gao et al. [17] developed a triboelectric metal-polymer plain bearing and demonstrated a way for identifying bearing lubrication states, with the test accuracy reaching 99.11%. Choi et al. [13] presented a triboelectric roller-bearing, which determines the differences in the electrical signals depending on the removed rollers, realizing the accurate monitoring for the number and positions of rollers. These researches establish the feasibility of self-diagnosis of triboelectric bearings aided by AI technology.

Although the TENG-based bearing sensors have been applied to various condition monitoring, the exploration of the rolling element detection of bearings is less. As a vulnerable component [24], the accurate diagnosis of rolling element defects is critical for the lifespan prediction and health monitoring of bearings. However, it raises a challenge to identify the partial defect of the rolling balls due to the similar output signals of triboelectric bearings in this case. While rolling, the bearing balls are also affected by the cage or inner and outer rings. Therefore, to obtain the defect information and distinguish the similar signals is valuable to be investigated further.

Herein, we directly install triboelectric assemblies in a commercial rolling bearing (T-bearing) to sense the defect of rolling balls and apply it to the fault diagnosis of bearings. Ensuring the

sufficient contact between the rolling ball and the triboelectric layer to obtain the contact-sensing signals is the key basis for detecting its defects. In this design, the flexible interdigitated copper electrodes covered with polytetrafluoroethylene (PTFE) dielectric film are attached to the inner surface of bearing outer ring as the triboelectric sensing layer. When the bearing rotates with the shaft, the electrical signal will be generated by the triboelectrification between the PTFE film and the steel balls, then output through the interdigitated electrodes. The direct contact between the steel ball and the sensing layer is more conducive to the contact electrification of the two mated friction pairs [25], resulting in a stable electrical signal with complete sensing information, which improves the sensitivity of T-bearing for the ball state change. To increase the SNR, the output voltage signal is determined to be utilized in this study. Even more, we firstly introduce a signal decomposition algorithm to extract features of the similar time-domain electrical signals caused by the ball defects. And ML is ordered to train these feature components containing fault information to classify and identify various defects. Combined with two algorithms, five kinds of working conditions of bearing balls are successfully detected and identified. The results show that the classification accuracy through extracting fault features by signal decomposition algorithm achieves more than 99.48%, which is much higher than that only by ML classification accuracy of the original signal of 78.34%. This study verifies the feasibility of triboelectric technology for bearing rolling element defect detection and the potential of AI algorithms in enhancing the precision of triboelectric sensors, thus showing excellent application prospects in the field of intelligent bearing.

2. Results and discussion

2.1. Structure and Working Principle of the T-bearing

The actual image of the T-bearing is shown in **Figure 1(a)**. The fabricated subject is a POM6310-type deep groove ball bearing, which provides a ready operation environment for the triboelectric assemblies [26]. **Figure 1(b)** shows the matching of the triboelectric sensing layer with the bearing to fabricate the prototype T-bearing. The triboelectric sensing layer, consisting of interdigitated copper electrodes and PTFE dielectric film, is the key to monitor rolling steel balls and sample electrical signals. As shown in **Figure 1(c)**, the copper electrodes are attached to the inside of the outer ring and PTFE film is covered on the electrodes. The number of interdigitated copper electrodes is designed to be twice rolling steel balls and keep uniform distribution to ensure the maximum stable output of T-bearing [12]. As can be seen in the assembled and exploded views in **Figure 1(b)** and **(d)**, the T-bearing is constituted of six parts, which are outer ring, inner ring, cage, rolling steel balls, PTFE dielectric film and interdigitated copper electrodes.

The inner ring of T-bearing rotates with the rotor, and the outer ring is fixed with the base. The cage can guide the movement of rolling balls, improve the internal lubrication of the bearing, and prevent the ball from falling off. Most of all, the cage evenly separates the rolling balls, so that each steel ball can roll normally between the inner and outer rings. Inner and outer rings, rolling balls and cage are the main components of a mechanical rolling bearing, which retain the structural integrity of T-bearing. The PTFE film and copper electrode are pasted on the inner surface of the outer ring, and form a rolling-type freestanding mode TENG with the steel balls, which can generate the most direct triboelectric signals that can reflect the defects. The thickness of the entire additional structure is 0.14 mm, it will be reduced if more suitable materials are available. The radial clearance of the original bearing is measured and confirmed to be 0.23 mm. The additional structure can be accommodated and does not hinder the normal operation of the bearing. Due to the forced extension of the flexible sensing layer, it fits more closely with the outer ring after the

steel ball rolled, and its thickness can be further reduced. The structural parameters of the fabricated T-bearing, as shown in **Supporting Information Figure S1**, are listed as follows: pitch diameter $D_m = 72.36$ mm, inner ring diameter $D_i = 50$ mm, rolling ball diameter $D_b = 11$ mm and contact angle $\alpha = 0^\circ$. The number of balls is $N_b = 11$. The number of interdigitated electrodes is $N_e = 22$ and the width is $W_e = 3$ mm.

The working principle of T-bearing is demonstrated in **Figure 1(e)** and **(f)**. Here, we idealize that steel balls are equidistant from each other by the isolation of the cage opening, and those balls are all aligned with the bottom copper electrode A or electrode B, which represent a pair of interdigitated electrodes. At the original stage **i**, after sufficiently contacting with the steel balls, the PTFE film is prone to get negative charges uniformly-distributed on the surface, leaving net positive charges on the steel balls, since PTFE is more triboelectrically negative than steel [27, 28]. At this moment, for balancing the potential, positive charges are electrostatically induced on electrode B without steel balls docking. The rotating of charged steel balls will propel charge flow from electrode B to electrode A through the external circuit, as displayed in stage **ii**, until a new electrostatic equilibrium is reached at stage **iii**. When the balls continue to rotate, charges move back from electrode A to electrode B, which is illustrated in stage **iv**, until returning to stage **i** again. Thus, an alternating current is generated in these cycles. The design of interdigitated electrodes facilitates the periodic charge for electricity transfer during the continuous rotating [12]. A recent report has pointed out that the attachment of a dielectric layer onto the electrode does not alter the changing trend of the electrical output [29]. It is worth mentioning that, although there is also a difference in electronegativity between steel and copper [30], the charge can be separated, but not as well as steel and PTFE. The selection of the covered PTFE dielectric film is also for special consideration, it not only provides insulation protection for the interdigitated electrode and

improves lubrication conditions in this design, but also has a mature production base in industry. The PTFE coating has been widely used as the self-lubricating layer of bearing inner wall because of its low friction coefficient, high temperature stability and excellent chemical resistance [31, 32]. Encouragingly, the ultra-wear-resistant triboelectric materials dedicated to bearings by Choi's group will make the combination of metal and polymer show a practical application prospect [17, 33].

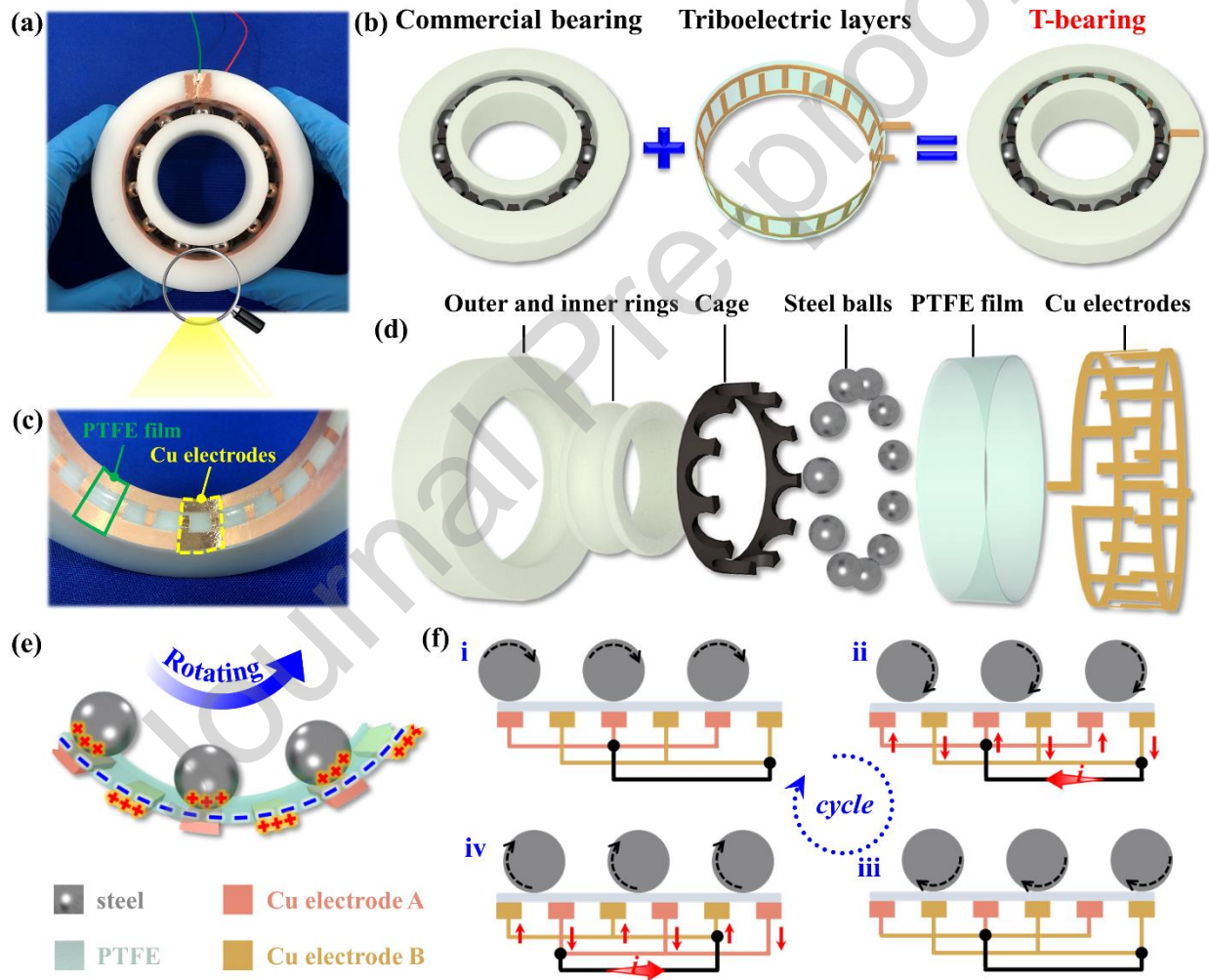


Figure 1. Structure and working principle of the T-bearing. (a) Actual photograph and (b) assembled view of the T-bearing. (c) Detailed photograph of the sensing layer. (d) Exploded view of the T-bearing. (e) Structural scheme and (f) working mechanism of the triboelectric sensing.

2.2. Electrical Characteristics and Output Performance of the T-bearing

The above charge flow process can be explained as the potential change between electrode A and B when the positively charged ball passes through under open circuit conditions. To verify the analyzed principle and visualize the voltage change of the T-bearing, the finite element method is employed to simulate the open-circuit voltage (V_{oc}) that varies with the rotation angle through COMSOL Multiphysics software. The simulated modeling restores the size of the actual T-bearing, which consists of eleven steel balls, a circle of PTFE layer and eleven pairs of interdigitated electrodes (each pair includes an electrode A and an electrode B), as shown in **Figure 2(a)**. The outer and inner ring are replaced by the air area. The potential distribution of the whole simulation model in the original stage is then displayed in **Figure 2(a)**. For a clear view of the continuous simulation process, **Figure 2(b)** shows the results of different stages corresponding to **Figure 1(f)** under the open-circuit condition. Within each step, the steel balls rotate 1 degree around the center of the bearing. Initially, as shown in stage **i**, a uniform distribution of negative charges on the PTFE layer, positive charges on the steel balls and electrode B. In the open-circuit condition, as the charges cannot transfer between electrodes without the load, the V_{oc} is defined as the electric potential difference between the two electrodes [34]. From this, electrode B obtains the maximum voltage while electrode A gets the minimum, resulting in the minimum output V_{oc} in the external circuit. With the rolling of steel balls caused by the rotating, the potential difference will increase to zero when the steel balls move from the original stage through 8° shown in stage **ii**. Then, in stage **iii**, the steel balls are brought to the position of electrode B after 16 steps, thus, the separation of the opposite charges will induce the maximum positive potential difference between electrode A and electrode B. Reversely, the potential difference decreases from the 16th

to 24th unit step (stage **iv**). Just as shown in **Figure 2(b)**, since the charges cannot really transfer in the simulation, the potential change of electrode A with the rotation of the steel balls is measured to refer to the change of V_{OC} . **Figure 2(c)** shows the qualitative relationship of the simulated V_{OC} with the rotation angle of steel balls. After sixteen unit steps (rotation angle= 16°), the highest potential differences are generated for both of the two structures from electrode A to electrode B. The simulation covers the entire one-circle rotating process that starts off from the initial position that the steel balls overlap with electrode A to the second position overlaps with electrode B, alternatively, until the end position that the steel balls rotate again to the initial position and overlap with electrode A, totally 360° . In the whole process, since eleven steel balls together (carried by the cage in real) pass through electrode A for a total of eleven times, and through electrode B for eleven times, theoretically the V_{OC} oscillates eleven times, as shown in **Supporting Information Figure S2**.

To characterize the electrical output performance of the T-bearing, a motor-driven rotor system with adjustable speed controlled by a frequency converter is established, as demonstrated in **Figure 2(d)**. The T-bearing and two companion bearings are installed on the main shaft, driven by the motor through the coupling. The T-bearing outer ring is mounted and fixed on a specially designed bearing chock to keep it in the center of the shaft. The electrical signal of the T-bearing is conducted by two wires connected to electrode A and electrode B. The signal acquisition flow is illustrated in **Figure 2(e)**, the output signal is measured by the electrometer and then transferred to the computer through a data acquisition (DAQ) unit. Firstly, the V_{OC} of T-bearing is acquired under the constant operating condition as the motor rotation speed is 60 rpm. As shown in **Figure 2(f)**, the waveform of V_{OC} oscillates with rotation as simulated (**Figure 2(c)**). However, due to the large noise interference ($f_{AC}=50.33$ Hz) from the power supply of the test system, the main

waveform of measured voltage is doped with higher-frequency fluctuations at a low rotation speed. Similar phenomenon is also mentioned in other works [14, 35, 36]. Subsequently, the measurements are performed under different rotation speeds. When the speed rises, the centrifugal force of the balls will overcome gravity, making close contact with the PTFE layer all the time [35], and the waveform of the voltage signal becomes smooth. Crucially, the impaction of the two matched triboelectric surfaces further enhances the contact perception [17]. The variation in the output waveform of V_{OC} is provided in **Supporting Information Figure S3** as the motor rotation speed varies from 60 to 600 rpm, respectively. According to the electric-generation mechanism of the freestanding mode TENG [34], the frequency of voltage waveform f_{Voc} is expressed as follows:

$$f_{Voc} = N \cdot f_{cage} \quad (1)$$

where $N=11$ is the number of interdigitated electrode pairs, and f_{cage} is the rotation frequency of the cage. Because being not fixed with the inner ring, the cage is not synchronized with the motor strictly. Considering the pure rolling mode, the relationship between the cage rotation frequency and inner ring rotation frequency f_{inner} can be calculated as follows [14, 16]:

$$f_{cage} = \frac{1}{2} f_{inner} \left(1 - \frac{D_b}{D_m} \cos \alpha\right) \quad (2)$$

As a deep groove ball bearing, $\alpha=0^\circ$. Substituting the structural parameters of T-bearing into Equation 2 yields $f_{cage}=0.43 \cdot f_{inner}$. **Figure 2(g)** shows that the V_{OC} increases from 29.5 to 40.7 V with the rotation speed increasing from 60 to 480 rpm, indicating a slow rising tendency. The main reason is that the contact area between the steel ball and PTFE film enhances in the wake of larger centrifugal force under higher rotation speed, which could also be found in the reference [16, 35]. Once exceeding 480 rpm, obviously, the stronger vibration is produced by the rotor system at higher speeds, affecting the running stability of the rolling element, resulting in weakened

electrostatic induction, which cause a decline in the V_{oc} , and the deterioration of signals can be known by the increase of error bars. This critical speed region can be verified by the previous reported triboelectric bearing [15]. The tested T-bearing has operated continuously for about 214 seconds at 480 rpm, over 1700 cycles, which still maintains a stable voltage output displayed in **Supporting Information Figure S4**. A cycle is when the main shaft driven by the motor turns around once. Finally, through all tests by one prototype, after running more than 31k cycles under different operating conditions, the voltage signal output has no obvious difference from the original signal, as shown in **Figure 2(h)**, thus proving the excellent durability of the T-bearing.

Journal Pre-proof

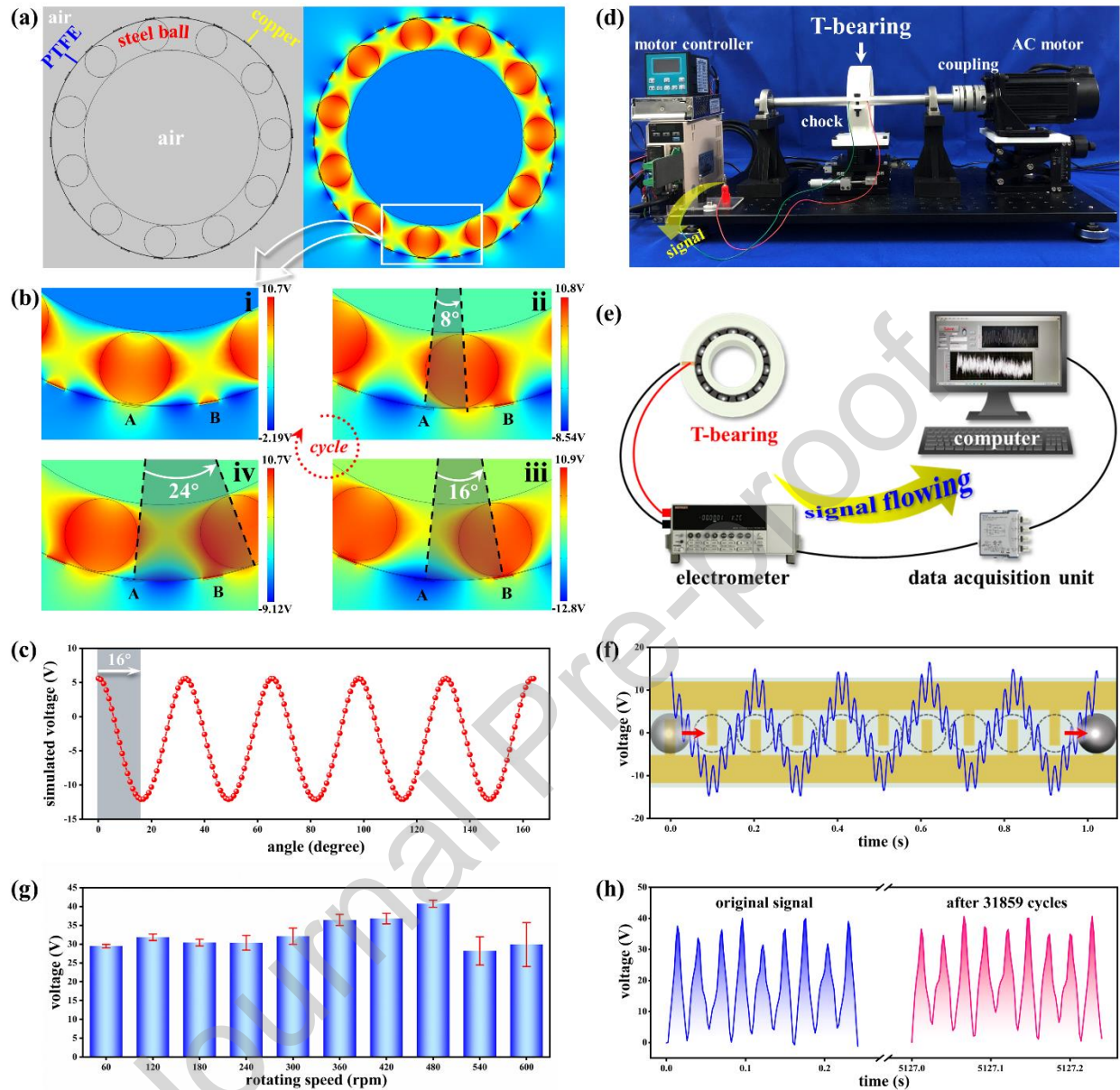


Figure 2. Theoretical model and experiment process of the T-bearing with rolling type free-standing mode. COMSOL simulation of (a) the initial setup and (b) periodic potential change between electrodes of the T-bearing. (c) Simulated V_{oc} in one circle rotating process. (d) Photograph of the measurement platform. (e) Flow of the data acquisition. (f) Measured V_{oc} of the T-bearing with the motor rotation speed of 60 rpm. (g) V_{oc} under different rotor speeds. (h)

Comparison of the original signal and the voltage signal after working 31859 cycles from the T-bearing.

Because the triboelectric signals can respond quickly to external changes, for severe abnormal stimuli, such as the start and stop of the excitation source [37], the mutation of the vibration frequency [22] or the rotation speed [35], some studies can successfully distinguish, including the related works of triboelectric bearings [14-16]. However, the research on the defect of bearing balls still needs to be improved. Here, the partial deletion of the sphere was introduced into and set as the rolling ball defect. The actual photographs of the defects on the steel balls are displayed in **Supporting Information Figure S5**. For the proposed T-bearing, the interdigitated electrodes will induce 22 times with the balls rotating a circle around the bearing center, which can easily record the change of ball's rolling state caused by its own morphology [12]. The fault details will be reflected in the time-domain signals and frequency-domain signals. In this study, the voltage signals from the T-bearing under 1 normal condition and 4 different fault conditions (one ball defect, two balls defect in opposite position, two balls defect in adjacent position, and PTFE dielectric film damage) with the highest stable speed of 480 rpm are collected as the original data to carry out the research. Considering that the sensing layer faces the risk of being worn by the steel balls, in addition to the ball defects, the extreme fault of the PTFE film damage is specially set up. And the signal samples belonging to 5 conditions are shown in **Figure 3(a) to (e)**. The partial defects of steel balls are not enough to delay the rotation of the T-bearing but will cause the collected voltage signal similar and confusable.

The Pearson correlation coefficients between the datasets of four voltage signals are analyzed in **Figure 3(f)**. The correlation heat map summarizes the strength of linear relationship between

the voltage signals [38]. The results show that four voltage signals are positively correlated with each other. Among them, the signals corresponding to normal condition, one ball defect and two balls defect in opposite position are with highly correlations (red area), and the coefficient is greater than 0.9, which are defined as the similar signals. As can be proved from the Pearson correlation of the similar signals, except in the extreme case with a broken dielectric layer, when the rotation speed is same and the sphere shape is changed little, it is difficult to recognize the difference between the time-domain signals from normal and ball defect conditions intuitively, nor the commonly used time-frequency transformation of the fast Fourier. It is worth mentioning that, the time length of the transformed original signal determines the resolution of the frequency, which will bring deviation in short-term and unfixed sampling [39]. In addition, whether it is a long-time data record or multiple repeated tests of the same TENG-based sensor, the signal offset and amplitude change are both common and unavoidable through the existing measurement methods. The offset of one experimental record is displayed in **Supporting Information Figure S6**. After two minutes of continuous measurement, the positive peak value of the voltage signal is shifted from 24 V to 42 V. The offset of multiple experiments can be seen by the different ranges of peak-to-peak values from each waveform shown in **Figure 3**. Most obviously, the normal voltage signal has been offset for a long time, ranging from -250 V to -200V. But the signal range corresponding to the two balls defect in adjacent position is 70 V to 110 V. Therefore, the defect diagnosis simply through the original signal, frequency and amplitude is unreliable [18].

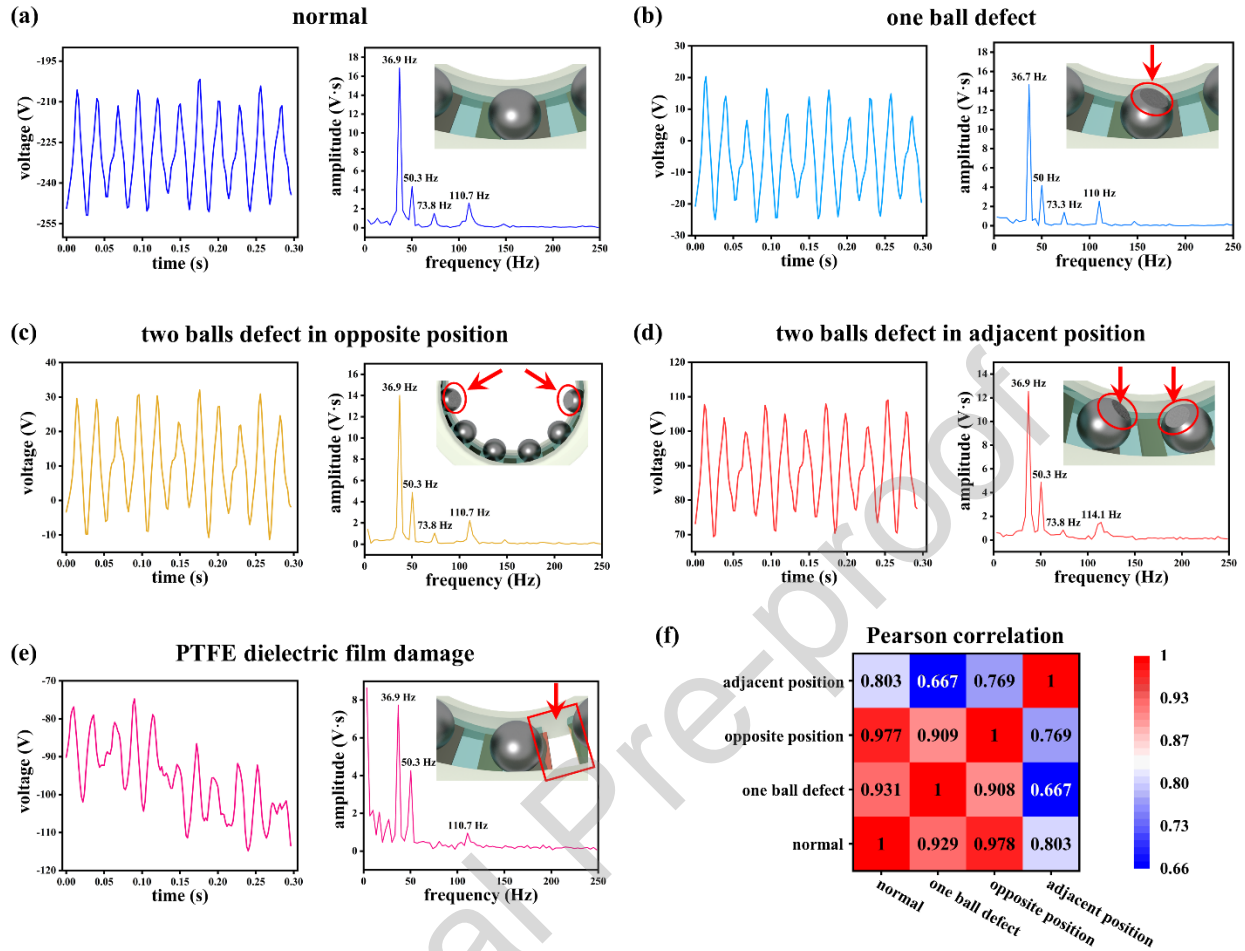


Figure 3. Time and frequency-domain comparison of voltage signals of the T-bearing with different faults: (a) normal, (b) one ball defect, (c) two balls defect in opposite position, (d) two balls defect in opposite position, and (e) PTFE dielectric film damage. (f) Correlation heat map of the similar signals.

2.3. Analysis and prediction framework for triboelectric signals

More and more attempts in mechanical fault diagnosis have proved that intelligent diagnosis methods combined with AI may replace time-consuming and unreliable human analysis, increasing the efficiency of diagnosis [22, 40]. Researchers have introduced ML, a common AI technique, into the field of fault diagnosis [41]. As a data-driven method, it has the advantage of

focusing only on the relationship between inputs and outputs without having to think too much about the physical processes involved. In ML, the input containing data type and data length, and the output are related to two most critical tasks. The output is directly determined by the prediction task for regression or classification. For example, in a regression task, the output predicted by the model is a series of values, which have the same physical meaning as the input data. And in a classification task, the output is a label that generally indicates the physical phenomenon or pattern behind the data. The input of the model affects its prediction performance. The existing prediction paradigm is basically using the collected original signal, and artificially setting a fixed value as input directly. This approach does not take the data heterogeneity into account, and the model cannot capture the key information. At the same time, in the field of mechanical fault diagnosis research, it usually belongs to the application of a single algorithm or model. However, no algorithm or model can perform well on all kinds of data. Because even after hyper-parameter optimization, the architecture capability of a single model is limited.

Herein, for the first time, the Seasonal and Trend decomposition using Loess (STL) and Automated machine learning (AutoML) are introduced to propose a new paradigm for the analysis and prediction of triboelectric signals. Bayesian optimization (BO) is also first applied to the dynamic optimization of the triboelectric signal recognition, which dynamically selects the best input length (number of sample points) and data features (data components). Specifically, STL is used for signal decomposition, AutoML is used for model prediction, and BO is responsible for optimization strategy.

The time series decomposition method STL is based on locally weighted scatterplot smoothing (Loess), which's core idea is to use Loess to smooth the time series data for decomposing into additive components, including seasonal, trend and remainder [42], as shown in **Figure 4(a)**. To

be specific, STL is made up of inner loop and outer loop, the inner loop is nested inside the outer loop [43]. The main steps of inner loop are seasonal smoothing and trend smoothing, after which, the trend values T_t and seasonal series S_t are got from the original values Y_t . And the remainder series R_t can be calculated according to Equation 3:

$$R_t = Y_t - T_t - S_t \quad (3)$$

Subtracting seasonal components from the original data, the results are smoothed with Loess, and the trend is obtained. The rest is remainder component. The mathematical details can be found in **Supporting Information Note S1**. As shown in **Figure 4(b)**, the original voltage signal is decomposed into three component features, and the dimension of data is extended from one to three. The seasonal component is regular changes in the development of phenomena caused by seasonality. The trend component refers to a trend or state of continuous development and change of phenomena over a long period of time. The irregular fluctuation in the remainder component refers to the influence of many accidental factors on time series. The components will bring more obvious defect-related features, rather than blindly adding the input of original signals. The features obtained from the post-processing are helpful for the model classification.

However, which feature is more helpful to the model performance among three components could not be determined at first. And it is also impossible to train for each existing situation, that is, the permutation and combination of three feature components and different input data lengths. Therefore, the BO algorithm is applied to optimize this problem and construct a new paradigm for electric signal analysis and prediction based on it.

BO is an iterative method for optimizing black-box functions, in which, the optimization problem is transformed into an inference of the probability model. Specifically, a prior distribution is advanced to represent the prior knowledge of the objective function, and updated by

continuously observing the value of the objective function to obtain a posterior distribution. The posterior distribution can be used to estimate the optimal solution of the objective function and guide the next optimization. The core of the BO algorithm is to select a point in each step to explore or utilize. The acquisition function balances exploration and utilization, and determines the location of the next exploration point. In this way, the algorithm can continuously explore new potential optimal solutions, and can also use the existing information to guide the search direction.

As a further principle explanation in **Figure 4(c)**, a randomly generated one-dimensional objective function, which is represented by green line, is optimized, and its global maximum is found. First, some sample points represented by red dots are initialized for cold start. Then we make a priori assumption on the unknown objective function distribution, as displayed in blue dotted line. The priori assumption usually chooses the Gaussian distribution, for it is the most widely used probabilistic surrogate model [44]. The blue shadow represents the confidence interval. Using expected improvement (EI) as the acquisition function, the value of the function is a dimensionless number, which indicates what points are more worth exploring. After the acquisition function gives the next most promising exploration point (black point), it is input into the objective function to obtain the return value. At the same time, the posterior distribution is modified to further moves closer to the objective function distribution. The optimal parameters obtained by optimization are output through iterations.

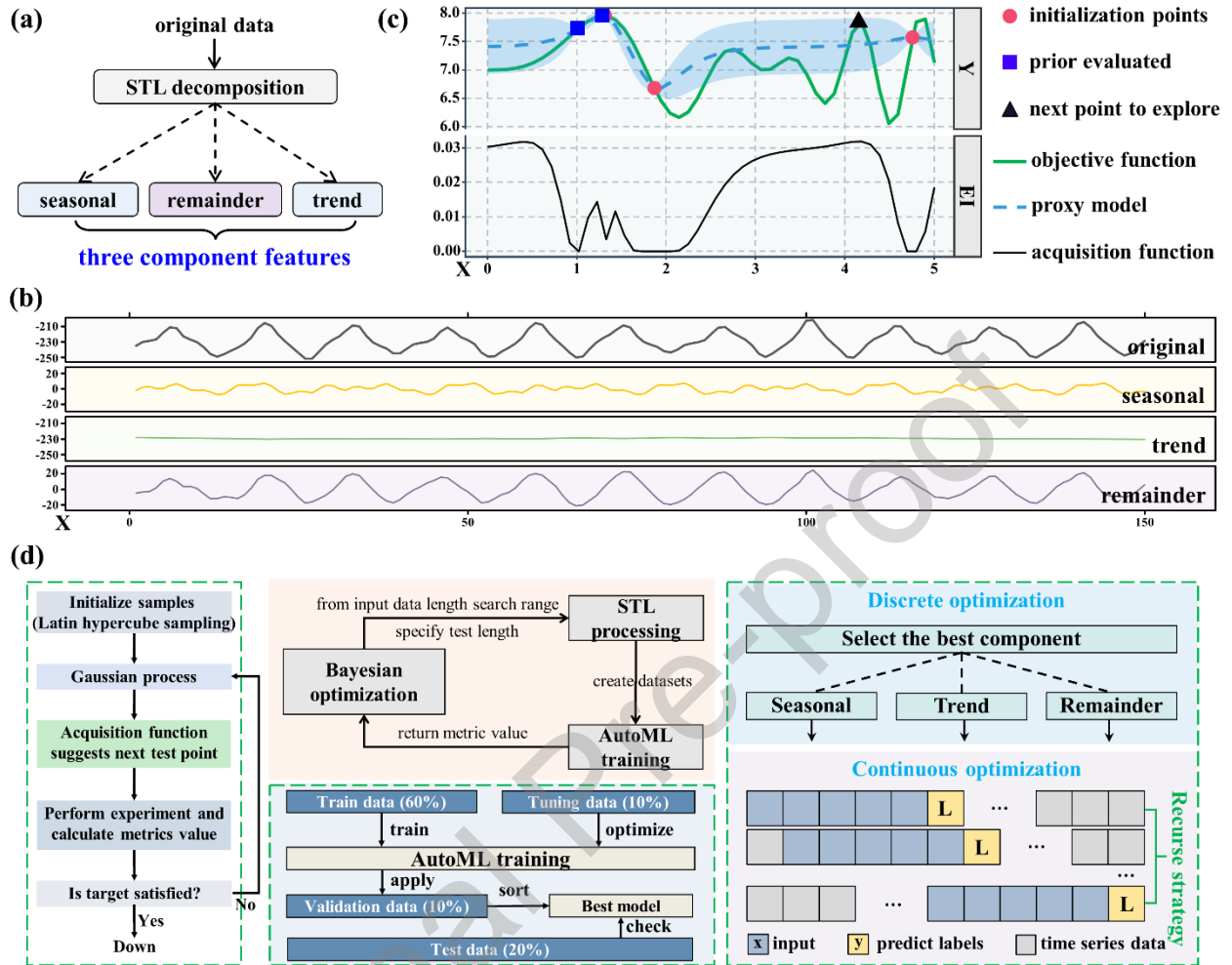


Figure 4. Analysis and prediction of triboelectric signals. (a) Schematic diagram of STL decomposition process. (b) Three feature search components of the T-bearing voltage signal decomposed through STL. (c) Visualization of BO process. (d) Direct-Recursive forecast framework consisting of AutoML and BO of lag features length.

Furthermore, AutoML, which is a novel model set paradigm, is applied for prediction model. In a given computing resource, i.e., time and hardware environment, the training and hyperparameter optimization of multiple models are automatically constructed, and the best model is returned according to the performance. It's worth noting that the training is highly automated, which is one

of the greatest advantages. After setting the stop index, the best model and corresponding hyperparameters are explored.

Based on STL, AutoML and BO, a new framework for the prediction of triboelectric signals is firstly proposed. As shown in **Figure 4(d)**, the BO algorithm is employed to dynamically optimize the input data length. The advantage of BO is that it does not need to exhaustively combine, but to explore the best parameter combination in as few times as possible. The search range of an input data length is first specified. The BO algorithm specializes in adjusting the length value, and then the corresponding data set is created. Among the seasonal, trend and remainder components decomposed from the original electrical signal through STL, only one is considered as the input data of the model, so the optimization of three components is discrete. Within each component, the input data length is continuously optimized. Then, AutoML serves as the prediction model to evaluate and return the metric value to BO. Through iterative optimization, the best input length and data features are dynamically selected by the BO algorithm.

2.4. Bearing Ball Defect Diagnosis with the T-bearing

Aiming at the acquired voltage signal data of T-bearing, the required parameters and settings before optimization should be specified. In this study, the voltage data was recorded with a sampling frequency of 500 Hz. One cycle voltage signal contains 15 sample points. Corresponds to select 4 to 20 signal cycles, the input data length is searched from 60 to 300 sample points. 50 sample points are initialized for cold start by the Latin Hypercube sampling method [45], and the number of iterations to 50 is set initially. The AutoML training time is set to 10 minutes and the stop indicator is log loss. All the trained models are sorted according to the mean per class error to get the model leaderboard. And the mean per class error is returned to BO as an evaluation index

of the parameter. Distributed Random Forest (DRF), Extremely Randomized Trees (XRT), Generalized Linear Model (GLM), Gradient Boosting Machine (GBM), Extreme Gradient Boosting (XGBoost), Deep learning (DL) and Stacked ensemble (SE) models are selected as the candidates for automated training. 70% of the data is used for training, 10% of which is used to optimize model parameters. 10% of the data is used for validation to generate the model leaderboard. 20% of the data is used to test the best model in leaderboard.

The visualizations of the 1st, 25th and 50th iterations are exhibited in **Figure 5(a)-(c)**, in which the processes of approximating the object function distribution and the state of the acquisition function are shown together. The red dots represent initialization. The blue squares represent points that have been explored before. The black triangles represent the most promising points to explore. It can be seen that after several iterations, the acquisition function gradually approaches the distribution of the objective function. Through comparing the object function, it is obvious that the remainder component is the greatest one to get the best prediction performance, while the trend component presents the worst. Exploring its source, for the voltage signal data of this study, as shown in **Figure 4(b)**, the seasonal component reflects the main movement of the ball, that is, the rotation around the shaft on the electrodes. The trend represents the deflection of the current signal range over a long period of time. On short datasets under constant speed, the above two components are similar, cannot provide representative information for different work conditions. The occasional anomalous observations do not affect the estimation of the trend and seasonal components, but ultimately, they will be counted in the remainder [46]. In theory, the remainder contains the fault information. Comparing the original data, because the redundant similar components are subtracted, the fault features are more prominent, which is helpful for the feature selection of the AutoML model.

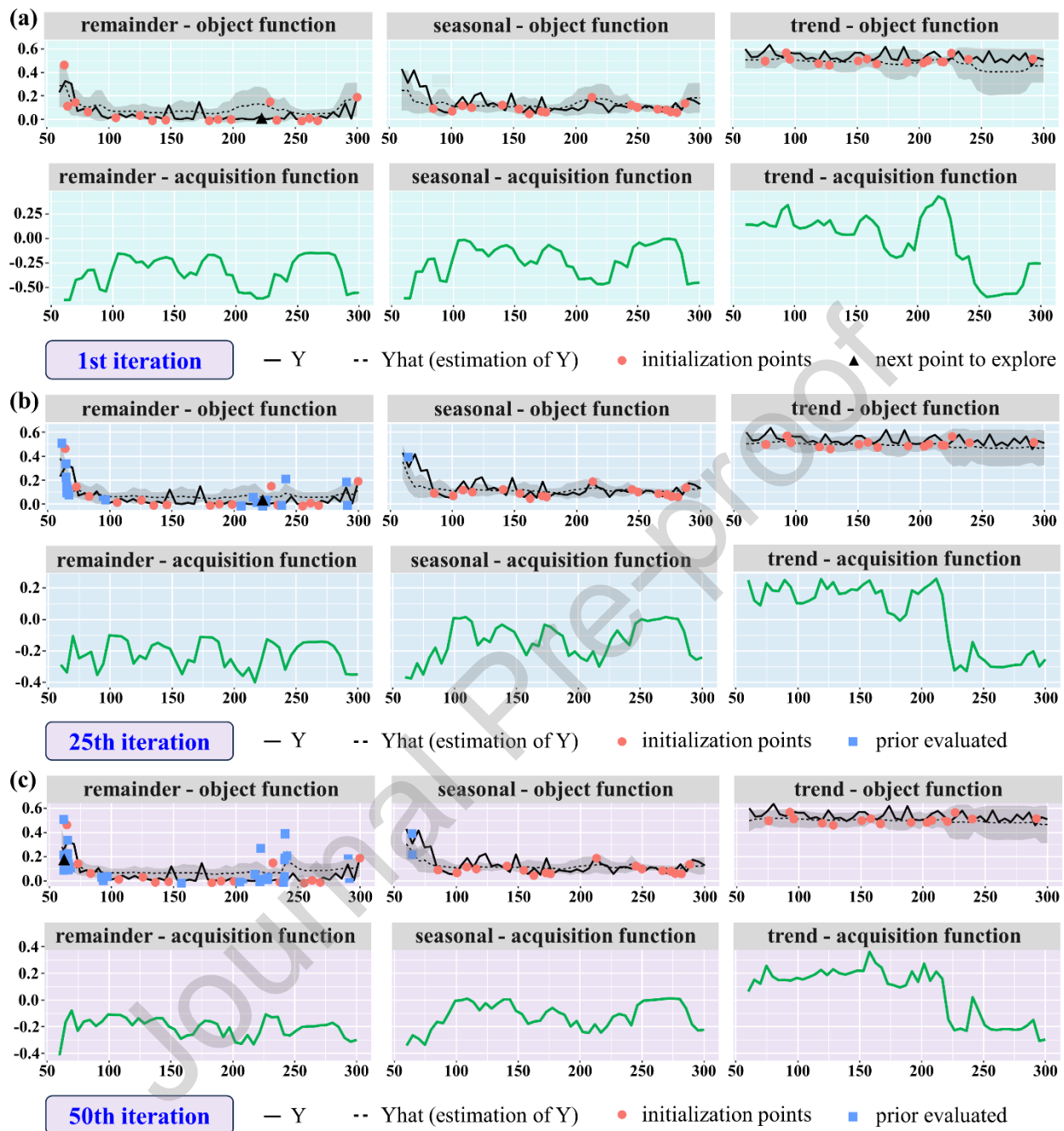


Figure 5. Processes of approaching the object function and state of the acquisition function. Visualization of (a) the 1st, (b) 25th and (c) 50th iterations.

More intuitively, the model accuracies of each feature component under different input data length are shown in **Figure 6(a)**. It can be clearly seen that the selection of feature components and input data length has a great influence on the prediction performance of the model.

It is worth noting that the above conclusions are the verification results obtained by exhausting all possible permutations and combinations as much as possible. In the dynamic optimization process, the proposed optimization framework does not determine in advance which component or which length works best. Adopting the exhaustive strategy, a total of 723 (3×241) groups need to be trained. Driven by the BO algorithm, the framework can search the best parameter combination as far as possible with much fewer attempts. Applying to the voltage signal of T-bearing, the final optimization result is shown in **Figure 6(b)**. The labels 1 to 5 corresponding to five working conditions are normal, one ball defect, two balls defect in opposite position, two balls defect in adjacent position, and PTFE dielectric film damage, respectively. In the framework proposed in this study, the remainder component is finally being determined as the input data and 156 sample points as the input length. Under the combination of the optimized parameters, the prediction accuracy of five different conditions with the best model trained by the framework is 99.48%. Only two samples are confused because the conditions represented by label 3 and 4 are both two balls defect just with different position distributions in the bearing. This also indicates that the proposed triboelectric signal prediction framework is capable of effectively selecting the best feature component type and the best input data length as the model inputs. Thus, the prediction performance of the model is guaranteed and improved without the exhaustive strategy.

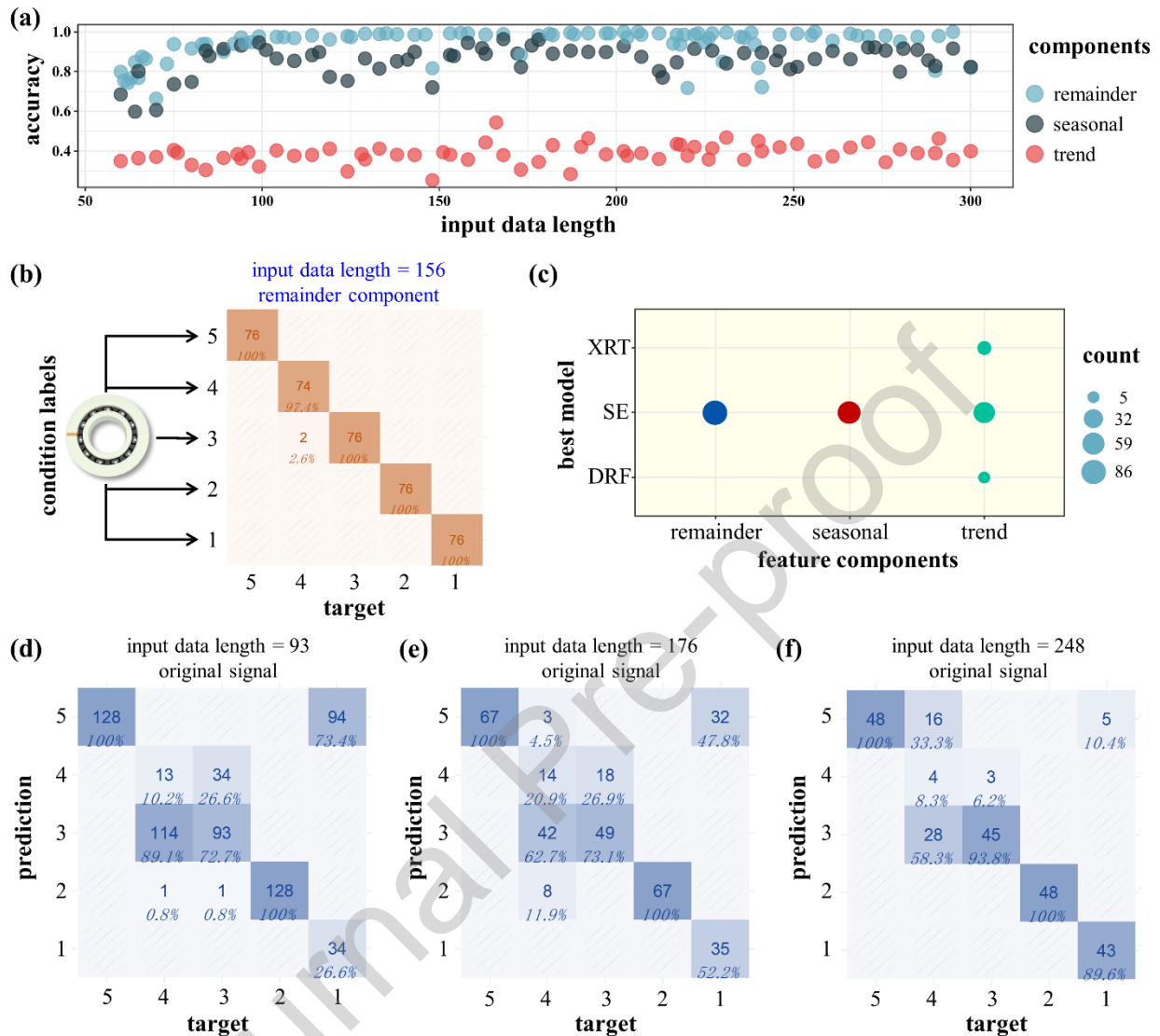


Figure 6. Prediction results of the AutoML model. (a) Model accuracies of each feature component under different input data length. (b) Prediction accuracy of SE model with the final optimization parameters. (c) Best model type distribution map from AutoML. (d), (e) and (f) Prediction accuracies to the original voltage signals with different input data lengths.

The best model type distribution map given by AutoML is shown in **Figure 6(c)**. Overall, the SE model performs best among three components. But for the trend component, the type of best model is not stable. This also implies that the trend component has uncertain feature law, which

will cause the extreme model performance. Finally, the ablation experiment is necessary. The original voltage signal of T-bearing is taken as input, and three input data lengths are randomly selected for verification. The ablation experiment remains the same as the parameters and settings in the previous dynamic optimization process of the framework, except that there is no decomposition step by STL. As shown in **Figure 6(d)** to **(f)**, without the intervention of the data decomposition algorithm, the prediction ability is always relatively poor. The reason is that it is difficult for the model to find robust classification features in the original voltage signals. The result of the ablation experiment verifies the excellent effectiveness of the proposed framework, introducing the STL algorithm for the first time to achieve accurate working condition recognition based on triboelectric signals.

3. Conclusions

In summary, a triboelectric sensor-embedded rolling bearing is fabricated and systematically investigated for the detection and recognition of rolling ball defects. The flexible interdigitated copper electrodes covered with PTFE dielectric film, which is attached on the inner surface of the bearing outer ring as the triboelectric sensing layer, exhibits the stable output performance and direct output signals. The output characteristics under various rotation speeds and the sensing signals under normal and fault conditions are measured and analyzed systematically. In view of the defect diagnosis of rolling balls, a new paradigm for the analysis and prediction of triboelectric signals is proposed, which achieves the dynamic selection of the optimal input length and data features. For the first time, the combination and cooperation of the STL decomposition, AutoML model and BO algorithm are developed for the similar triboelectric signals analysis obtained during the test of T-bearing. The STL is introduced to extract the features of similar time-domain

voltage signals caused by the bearing ball defects. The AutoML model is used to train the feature components containing fault information to complete the classification and identification of normal working condition and different faults. With the BO algorithm applied to the dynamic optimization of parameters, the recognition accuracy of five different conditions with the best model is 99.48 %, which is extremely superior to the highest accuracy of 78.34% without signal decomposition. Therefore, this study intelligentizes the existing bearings and improves the accuracy of fault diagnosis based on triboelectric signals that are easily affected by the environment.

Although obtaining the triboelectric signals that can reflect the defects, the proposed sensing layer is in direct contact with the rolling steel balls. It will carry a risk of wear and bring additional vibration to the bearing operating. In future work, the robustness of the structure design to real scenarios is worth studying.

4. Experiments

4.1. Fabrication of the T-bearing

The T-bearing consists of a POM6310-type deep groove ball bearing, a PTFE dielectric film with a thickness of 0.08 mm, and interdigitated copper electrodes with a thickness of 0.06 mm. The plastic rolling bearings with steel balls were purchased from KIF BEARINGS Company and its structural parameters were shown in **Supporting Information Figure S1**. The PTFE film with back glue was used as the electronegative triboelectric layer. The flexible interdigitated electrodes consist of two group of complimentary finger arrays, each of which has eleven electrode fingers. The spacing between two adjacent fingers was approximately 8.3 mm and the finger width was 3 mm. Then, the design shape was printed on the surface of the copper tape. The interdigitated

electrodes were obtained by cutting the copper tape. After cleaning and drying the bearing, the interdigitated copper electrodes were attached to the inner surface of outer ring. The PTFE film with a width of 27 mm is covered on the electrodes to protect the internal structure because of its strong insulativity and good flexibility. Above these, the T-bearing was completed and its effective triboelectric area is 125.31 cm².

4.2. Setting of the bearing faults

Following the common method of fault simulation experiments [47], the metal cutting technology was used to introduce three kinds of ball defect faults: one ball defect, two balls defect in opposite position and two balls defect in adjacent position. In order to characterize the degree of defect, we weighed the normal ball and the defect ball, which respectively is 5.46 g and 5.27 g. The cut weight is about 3% of a normal ball to simulate the partial defect. The extreme failure condition was introduced by cutting a bare surface of 16 mm × 27 mm on the PTFE film. Details of faults were shown in **Supporting Information Figure S5**.

4.3. Establishment of variable rotation speed test bench

The test bench consisted of an AC servo motor (HeChuang, 750 W, 6000 rpm), frequency converter (DKC-Y110), rotor shaft (aluminum alloy, diameter 17 mm, length 360 mm) and bearing pedestal (SKP003, inner diameter 17 mm). All the test components were bolted to the optical platform (aluminum, 600mm × 300mm × 13mm). The T-bearing was supported by two pedestals.

4.4. Signal measurement and postprocessing

The open-circuit voltage of T-bearing was measured using an electrometer high resistance meter (Keithley 6514) and an analog-to-digital converter (NI 9215). The voltage data was sent to the LabView software-based computer with a sampling frequency of 500 Hz. The data postprocessing are implemented by RStudio and Origin 2019b.

Declaration of competing interest

The authors declare that they have no known competing financial interests or personal relationships that could have appeared to influence the work reported in this paper.

Data availability

Data will be made available on request.

Acknowledgments

The work is supported by the National Natural Science Foundation of China (Grant Nos.52101345, 52101400), Scientific Research Fund of the Educational Department of Liaoning Province (Grant No. LJKZ0055), Dalian Outstanding Young Scientific and Technological Talents Project (2021RJ11), the Open Fund of National Center for International Research of Subsea Engineering Technology and Equipment (No. 3132023354).

Appendix A. Supporting information

Supplementary material related to this article can be found in the online version.

References

- [1] A. K. S. Jardine, D. M. Lin, D. Banjevic, A review on machinery diagnostics and prognostics implementing condition-based maintenance, *Mech. Syst. Signal Proc.* 20 (2006) 1483-1510, <http://doi.org/10.1016/j.ymssp.2005.09.012>.
- [2] R. N. Liu, B. Y. Yang, E. Zio, X. F. Chen, Artificial intelligence for fault diagnosis of rotating machinery: A review, *Mech. Syst. Signal Proc.* 108 (2018) 33-47, <http://doi.org/10.1016/j.ymssp.2018.02.016>.
- [3] M. Cerrada, R. V. Sanchez, C. Li, F. Pacheco, D. Cabrera, J. V. de Oliveira, R. E. Vasquez, A review on data-driven fault severity assessment in rolling bearings, *Mech. Syst. Signal Proc.* 99 (2018) 169-196, <http://doi.org/10.1016/j.ymssp.2017.06.012>.
- [4] Y. Jin, R. Gao, R. Warrington Microcomputer-based real-time bearing monitor, 1993 IEEE Instrumentation and Measurement Technology Conference, IEEE: 709-714.
- [5] B. T. Holm-Hansen, R. X. Gao Smart bearing utilizing embedded sensors: design considerations, *Smart Structures and Materials 1997: Smart Structures and Integrated Systems*, SPIE: 602-610.
- [6] F. R. Fan, Z. Q. Tian, Z. L. Wang, Flexible triboelectric generator!, *Nano Energy* 1 (2012) 328-334, <http://doi.org/10.1016/j.nanoen.2012.01.004>.
- [7] T. L. Du, F. Y. Dong, Z. Y. Xi, M. X. Zhu, Y. J. Zou, P. T. Sun, M. Y. Xu, Recent Advances in Mechanical Vibration Energy Harvesters Based on Triboelectric Nanogenerators, *Small* 19 (2023) 27, <http://doi.org/10.1002/sml.202300401>.
- [8] Y. J. Zou, J. P. Wang, Z. Y. Hu, M. Z. Sun, J. H. Liu, T. L. Du, P. T. Sun, M. Y. Xu, Advances in Triboelectric Flow Sensor, *Adv. Mater. Technol.* (2023) 20, <http://doi.org/10.1002/admt.202300316>.

- [9] Y. Wu, Q. S. Jing, J. Chen, P. Bai, J. J. Bai, G. Zhu, Y. J. Su, Z. L. Wang, A Self-Powered Angle Measurement Sensor Based on Triboelectric Nanogenerator, *Adv. Funct. Mater.* 25 (2015) 2166-2174, <http://doi.org/10.1002/adfm.201403828>.
- [10] Q. F. Shi, Z. D. Sun, Z. X. Zhang, C. Lee, Triboelectric Nanogenerators and Hybridized Systems for Enabling Next-Generation IoT Applications, *Research 2021* (2021) 30, <http://doi.org/10.34133/2021/6849171>.
- [11] X. S. Meng, H. Y. Li, G. Zhu, Z. L. Wang, Fully enclosed bearing-structured self-powered rotation sensor based on electrification at rolling interfaces for multi-tasking motion measurement, *Nano Energy* 12 (2015) 606-611, <http://doi.org/10.1016/j.nanoen.2015.01.015>.
- [12] X. H. Li, C. B. Han, T. Jiang, C. Zhang, Z. L. Wang, A ball-bearing structured triboelectric nanogenerator for nondestructive damage and rotating speed measurement, *Nanotechnology* 27 (2016) 9, <http://doi.org/10.1088/0957-4484/27/8/085401>.
- [13] D. Choi, T. Sung, J. Y. Kwon, A Self-Powered Smart Roller-Bearing Based on a Triboelectric Nanogenerator for Measurement of Rotation Movement, *Adv. Mater. Technol.* 3 (2018) 8, <http://doi.org/10.1002/admt.201800219>.
- [14] Q. K. Han, Z. Ding, Z. Y. Qin, T. Y. Wang, X. P. Xu, F. L. Chu, A triboelectric rolling ball bearing with self-powering and self-sensing capabilities, *Nano Energy* 67 (2020) 10, <http://doi.org/10.1016/j.nanoen.2019.104277>.
- [15] S. Gao, Q. K. Han, X. N. Zhang, P. Pennacchi, F. L. Chu, Ultra-high-speed hybrid ceramic triboelectric bearing with real-time dynamic instability monitoring, *Nano Energy* 103 (2022) 13, <http://doi.org/10.1016/j.nanoen.2022.107759>.

- [16] Z. Y. Jiang, S. Gao, Y. Kong, P. Pennacchi, F. L. Chu, Q. K. Han, Ultra-compact triboelectric bearing based on a ribbon cage with applications for fault diagnosis of rotating machinery, *Nano Energy* 99 (2022) 10, <http://doi.org/10.1016/j.nanoen.2022.107263>.
- [17] M. Gao, T. D. Sun, Y. H. Li, Z. X. Zhang, C. K. Lee, J. Choi, AI-Enabled Metal-Polymer Plain Bearing Based on the Triboelectric Principle, *Adv. Funct. Mater.* (2023) 11, <http://doi.org/10.1002/adfm.202304070>.
- [18] Q. F. Shi, Z. X. Zhang, T. Y. Y. He, Z. D. Sun, B. J. Wang, Y. Q. Feng, X. C. Shan, B. Salam, C. Lee, Deep learning enabled smart mats as a scalable floor monitoring system, *Nat. Commun.* 11 (2020) 11, <http://doi.org/10.1038/s41467-020-18471-z>.
- [19] T. Jin, Z. D. Sun, L. Li, Q. Zhang, M. L. Zhu, Z. X. Zhang, G. J. Yuan, T. Chen, Y. Z. Tian, X. Y. Hou, C. Lee, Triboelectric nanogenerator sensors for soft robotics aiming at digital twin applications, *Nat. Commun.* 11 (2020) 12, <http://doi.org/10.1038/s41467-020-19059-3>.
- [20] Z. X. Zhang, F. Wen, Z. D. Sun, X. G. Guo, T. Y. Y. He, C. K. Lee, Artificial Intelligence-Enabled Sensing Technologies in the 5G/Internet of Things Era: From Virtual Reality/Augmented Reality to the Digital Twin, *Adv. Intell. Syst.* 4 (2022) 23, <http://doi.org/10.1002/aisy.202100228>.
- [21] Z. X. Zhang, L. W. Wang, C. K. Lee, Recent Advances in Artificial Intelligence Sensors, *Adv. Sensor Res.* 2 (2023) 2200072, <http://doi.org/https://doi.org/10.1002/adsr.202200072>.
- [22] H. F. Zhao, M. R. Shu, Z. H. Ai, Z. R. Lou, K. W. Sou, C. Y. Lu, Y. C. Jin, Z. H. Wang, J. Y. Wang, C. S. Wu, Y. D. Cao, X. M. Xu, W. B. Ding, A Highly Sensitive Triboelectric Vibration Sensor for Machinery Condition Monitoring, *Adv. Energy Mater.* 12 (2022) 11, <http://doi.org/10.1002/aenm.202201132>.

- [23] Q. K. Han, Z. Y. Jiang, X. P. Xu, Z. Ding, F. L. Chu, Self-powered fault diagnosis of rolling bearings based on triboelectric effect, *Mech. Syst. Signal Proc.* 166 (2022) 14, <http://doi.org/10.1016/j.ymssp.2021.108382>.
- [24] M. D. Marko, The Impact of Lubricant Film Thickness and Ball Bearings Failures †, *Lubricants* 7 (2019) 12, <http://doi.org/10.3390/lubricants7060048>.
- [25] X. Liu, J. J. Zhang, L. Q. Zhang, Y. G. Feng, M. Feng, N. Luo, D. A. Wang, Influence of interface liquid lubrication on triboelectrification of point contact friction pair, *Tribol. Int.* 165 (2022) 8, <http://doi.org/10.1016/j.triboint.2021.107323>.
- [26] F. Shen, Z. J. Li, C. F. Xin, H. Y. Guo, Y. Peng, K. Li, Interface Defect Detection and Identification of Triboelectric Nanogenerators via Voltage Waveforms and Artificial Neural Network, *ACS Appl. Mater. Interfaces* 14 (2022) 3437-3445, <http://doi.org/10.1021/acsami.1c19718>.
- [27] H. Y. Zou, Y. Zhang, L. T. Guo, P. H. Wang, X. He, G. Z. Dai, H. W. Zheng, C. Y. Chen, A. C. Wang, C. Xu, Z. L. Wang, Quantifying the triboelectric series, *Nat. Commun.* 10 (2019) 9, <http://doi.org/10.1038/s41467-019-09461-x>.
- [28] L. Lin, Y. N. Xie, S. M. Niu, S. H. Wang, P. K. Yang, Z. L. Wang, Robust Triboelectric Nanogenerator Based on Rolling Electrification and Electrostatic Induction at an Instantaneous Energy Conversion Efficiency of similar to 55%, *ACS Nano* 9 (2015) 922-930, <http://doi.org/10.1021/nn506673x>.
- [29] Z. T. Chen, K. R. Dai, J. X. Chen, J. T. Zhuo, D. N. Zhao, R. Ma, X. J. Zhang, X. B. Li, X. F. Wang, G. W. Yang, F. Yi, Influence of the Reference Electrode on the Performance of Single-Electrode Triboelectric Nanogenerators and the Optimization Strategies, *Adv. Sci.* 10 (2023) 13, <http://doi.org/10.1002/advs.202206950>.

[30] Q. Z. Sun, F. Liang, G. Z. Ren, L. R. Zhang, S. H. He, K. Gao, Z. Y. Gong, Y. L. Zhang, X. Kang, C. C. Zhu, Y. X. Song, H. X. Sheng, G. Lu, H. D. Yu, W. Huang, Density-of-States Matching-Induced Ultrahigh Current Density and High-Humidity Resistance in a Simply Structured Triboelectric Nanogenerator, *Adv. Mater.* 35 (2023) 9, <http://doi.org/10.1002/adma.202210915>.

[31] V. Saisnith, V. Fridrici, A study of the wear damage of a PTFE coating: The effects of temperature and environment on its mechanical and tribological properties, *Wear* 480 (2021) 9, <http://doi.org/10.1016/j.wear.2021.203946>.

[32] J. Wang, X. R. Huang, W. Wang, H. S. Han, H. Y. Duan, S. L. Yu, M. F. Zhu, Effects of PTFE coating modification on tribological properties of PTFE/aramid self-lubricating fabric composite, *Mater. Res. Express* 9 (2022) 10, <http://doi.org/10.1088/2053-1591/ac587a>.

[33] M. Gao, Y. H. Li, J. Choi, Triboelectric pad journal bearing for self-powered condition monitoring, *Nano Energy* 103 (2022) 10, <http://doi.org/10.1016/j.nanoen.2022.107851>.

[34] Y. N. Xie, S. H. Wang, S. M. Niu, L. Lin, Q. S. Jing, J. Yang, Z. Y. Wu, Z. L. Wang, Grating-Structured Freestanding Triboelectric-Layer Nanogenerator for Harvesting Mechanical Energy at 85% Total Conversion Efficiency, *Adv. Mater.* 26 (2014) 6599-6607, <http://doi.org/10.1002/adma.201402428>.

[35] T. L. Du, F. Y. Dong, M. X. Zhu, Z. Y. Xi, F. M. Li, Y. J. Zou, P. T. Sun, M. Y. Xu, Self-Powered and Robust Marine Exhaust Gas Flow Sensor Based on Bearing Type Triboelectric Nanogenerator, *J. Mar. Sci. Eng.* 10 (2022) 13, <http://doi.org/10.3390/jmse10101416>.

[36] Z. J. Xie, J. W. Dong, Y. J. Li, L. Gu, B. Y. Song, T. H. Cheng, Z. L. Wang, Triboelectric rotational speed sensor integrated into a bearing: A solid step to industrial application, *Extreme Mech. Lett.* 34 (2020) 8, <http://doi.org/10.1016/j.eml.2019.100595>.

- [37] T. L. Du, X. S. Zuo, F. Y. Dong, S. Q. Li, A. E. Mtui, Y. J. Zou, P. Zhang, J. H. Zhao, Y. W. Zhang, P. T. Sun, M. Y. Xu, A Self-Powered and Highly Accurate Vibration Sensor Based on Bouncing-Ball Triboelectric Nanogenerator for Intelligent Ship Machinery Monitoring, *Micromachines* 12 (2021) 14, <http://doi.org/10.3390/mi12020218>.
- [38] L. L. Zu, J. Wen, S. B. Wang, M. Zhang, W. L. Sun, B. D. Chen, Z. L. Wang, Multiangle, self-powered sensor array for monitoring head impacts, *Sci. Adv.* 9 (2023) 11, <http://doi.org/10.1126/sciadv.adg5152>.
- [39] A. Akan, O. K. Cura, Time-frequency signal processing: Today and future, *Digit. Signal Prog.* 119 (2021) 16, <http://doi.org/10.1016/j.dsp.2021.103216>.
- [40] S. R. Saufi, Z. A. Bin Ahmad, M. S. Leong, M. H. Lim, Gearbox Fault Diagnosis Using a Deep Learning Model With Limited Data Sample, *IEEE Trans. Ind. Inform.* 16 (2020) 6263-6271, <http://doi.org/10.1109/tii.2020.2967822>.
- [41] Y. G. Lei, B. Yang, X. W. Jiang, F. Jia, N. P. Li, A. K. Nandi, Applications of machine learning to machine fault diagnosis: A review and roadmap, *Mech. Syst. Signal Proc.* 138 (2020) 39, <http://doi.org/10.1016/j.ymsp.2019.106587>.
- [42] R. B. Cleveland, W. S. Cleveland, J. E. McRae, I. J. J. O. S. Terpenning, STL: A Seasonal Trend Decomposition Procedure Based on LOESS, *J. Off. Stat.* 6 (1990) 3-73.
- [43] D. W. Chen, J. H. Zhang, S. X. Jiang, Forecasting the Short-Term Metro Ridership With Seasonal and Trend Decomposition Using Loess and LSTM Neural Networks, *IEEE Access* 8 (2020) 91181-91187, <http://doi.org/10.1109/access.2020.2995044>.
- [44] X. Wang, Y. Jin, S. Schmitt, M. Olhofer, Recent Advances in Bayesian Optimization, *ACM Comput. Surv.* 55 (2023) 287, <http://doi.org/10.1145/3582078>.

[45] H. Y. Yang, H. Wang, Y. Y. Gao, X. Y. Liu, M. Y. Xu, A significant wave height forecast framework with end-to-end dynamic modeling and lag features length optimization, *Ocean Eng.* 266 (2022) 13, <http://doi.org/10.1016/j.oceaneng.2022.113037>.

[46] E. B. Dagum, S. Bianconcini, *Seasonal adjustment methods and real time trend-cycle estimation*. Springer: 2016.

[47] C. Lessmeier, J. K. Kimotho, D. Zimmer, W. Sextro Condition Monitoring of Bearing Damage in Electromechanical Drive Systems by Using Motor Current Signals of Electric Motors: A Benchmark Data Set for Data-Driven Classification, *European Conference of the Prognostics and Health Management Society*, 2016, URL <http://mb.uni-paderborn.de/kat/datacenter>.

Biographies



Fangyang Dong received his B.S. from Dalian Maritime University in China in 2019. Currently, he is as a postgraduate student in Marine Engineering College, Dalian Maritime University. His current research work focuses on Triboelectric Nanogenerator and artificial intelligence algorithm.



Hengyi Yang received his B.S. degree from Dalian Maritime University, China in 2021. Now he is a M.S. student at Dalian Maritime University. His main research interests include machine learning in energy and biorobots.



Hengxu Du received his B.S. in 2021. Currently, he is as a postgraduate student in Marine Engineering College, Dalian Maritime University. His current research work focus on Triboelectric Nanogenerator and Hydrodynamics.



Meixian Zhu received his B.S. in 2019. Currently, he is as a postgraduate student in Marine Engineering College, Dalian Maritime University. His current research work focus on Triboelectric Nanogenerator and artificial intelligence algorithm.



Ziyue Xi received his B.S. in 2021. Currently, he is as a postgraduate student in Marine Engineering College, Dalian Maritime University. His current research work focus on Triboelectric Nanogenerator and artificial intelligence algorithm.



Yulian Wang received her B.S. in 2022. Currently, she is as a postgraduate student in Marine Engineering College, Dalian Maritime University. Her current research work focus on Triboelectric Nanogenerator and artificial intelligence algorithm.



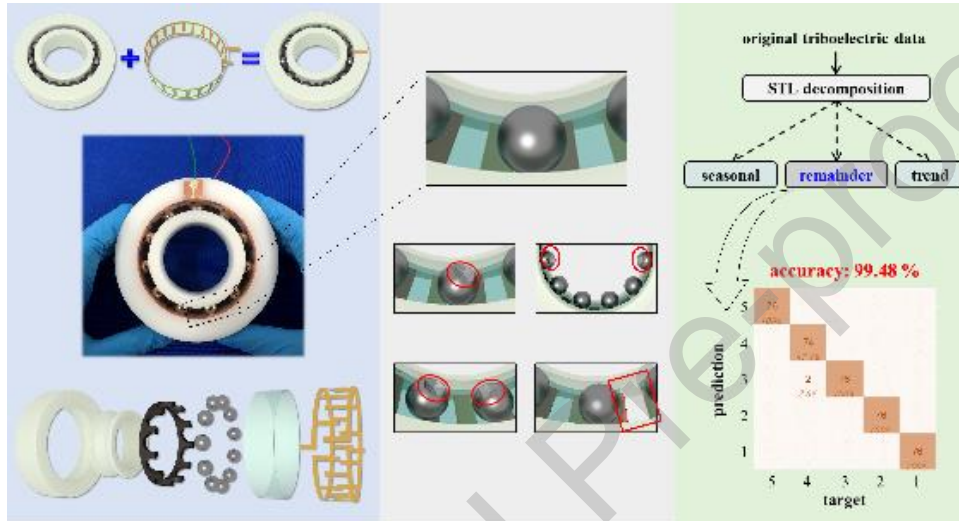
Taili Du has been with Dalian Maritime University where he is currently an Associate Professor since 2010. He received his B.S. and M.S. from Dalian Maritime University in China in 2008 and 2010, and he is as a doctoral candidate in Marine Engineering College, Dalian Maritime University. His current research work focuses on vibration energy harvesting and self-powered vibration sensor based on Triboelectric Nanogenerator.



Minyi Xu received his Ph.D. degree from Peking University in 2012. During 2016–2017, he joined Professor Zhong Lin Wang’ group at Georgia Institute of Technology. Now he is a Professor in the Marine Engineering College, Dalian Maritime University. His current research is mainly focused on the areas of blue energy, self-powered systems, triboelectric nanogenerators and its practical applications in smart ship and ocean.

Graphical Abstract

Through extracting fault features by signal decomposition, the machine learning classification accuracies of Triboelectric Nanogenerator-embedded intelligent bearing with five working conditions of normal status and rolling ball defects can reach more than 99.48%.



CRedit authorship contribution statement

Fangyang Dong: Conceptualization, Methodology, Software, Formal analysis, Investigation, Data Curation, Writing - Original Draft, Visualization, Project administration.

Hengyi Yang: Conceptualization, Methodology, Software, Formal analysis, Investigation, Data Curation, Writing - Original Draft, Visualization.

Hengxu Du: Investigation, Resources, Data Curation.

Meixian Zhu: Investigation, Resources, Data Curation.

Ziyue Xi: Resources, Visualization.

Yulian Wang: Software, Data Curation.

Taili Du: Writing - Review & Editing, Supervision, Project administration, Funding acquisition.

Minyi Xu: Writing - Review & Editing, Supervision, Project administration, Funding acquisition.

Declaration of interests

The authors declare that they have no known competing financial interests or personal relationships that could have appeared to influence the work reported in this paper.

The authors declare the following financial interests/personal relationships which may be considered as potential competing interests:

Highlights

- A flexible film triboelectric sensor is designed for commercial bearings, attaching in the bearing outer ring to sense the state of rolling balls.
- A new framework is proposed for the analysis and prediction of similar triboelectric signals generated by weak disturbances.
- The fabricated triboelectric bearing achieves the diagnosis of rolling ball defects by signal decomposition and automated machine learning.